Available online at www.sciencedirect.com
ScienceDirect
Trans. Nonferrous Met. Soc. China 33(2023) 2631−2645
Transactions of Nonferrous Metals Society of China
www.tnmsc.cn

Synthesis of ZIF-67 film in micro-arc oxidation anticorrosion coating on AZ31 magnesium alloy

Yong-hua CHEN[1,2], Liang WU[1,2], Wen-hui YAO[1,2], Yan-ning CHEN[1,2],
Jia-hao WU[1,2], Yuan YUAN[1,2], Bin JIANG[1,2], Andrej ATRENS[3], Fu-sheng PAN[1,2]

1. National Engineering Research Center for Magnesium Alloys, College of Materials Science and Engineering, Chongqing University, Chongqing 400044, China;
2. State Key Laboratory of Mechanical Transmission, Chongqing University, Chongqing 400044, China;
3. School of Mechanical and Mining Engineering, The University of Queensland, Brisbane Qld 4072, Australia

Received 17 June 2022; accepted 7 December 2022

Abstract: In order to improve the corrosion resistance of AZ31 magnesium (Mg) alloy and the adhesion of metal-organic frameworks (MOFs) coating, a MAO/ZIF-67 (Co-based MOFs) (micro arc oxide/ZIF-67) composite coating was fabricated by in-situ growth on AZ31 MAO coating. The results showed that ZIF-67 with rhombic dodecahedron uniformly grew on the surface of MAO coating, and exhibited good adhesion to the substrate, which made MAO/ZIF-67 composite coating have good corrosion resistance. It was proved that ZIF-67 could effectively seal the pores of MAO coating, increase the tortuosity of the invasion path of corrosion medium, and significantly improve the corrosion resistance of Mg alloy. In addition, MAO pretreatment gave the coating strong adhesion, which was more conducive to ZIF-67 sealing micro-pores. This study is of great significance to reduce the limitation of MOF coating applied to all metal substrates.

Key words: metal-organic framework; ZIF-67; micro-arc oxidation; anticorrosion; coating; Mg−Al−Zn alloy

1 Introduction

As the most developed and potential “green engineering material” in the 21st century, magnesium (Mg) has the advantages of low density, high specific strength, good electrical and thermal conductivity, good machinability, and low cost [1]. Mg and its alloys (commonly Mg−Al−Zn alloy, also known as AZ31) have been widely used in automobile manufacturing, electronic communication, aerospace, military and nuclear energy and other industrial fields [1,2]. However, Mg has high chemical activity, so Mg and its alloys are prone to corrosion [3], including premature loss of mechanical properties, local pH increase, and massive hydrogen evolution [4]. Thus, controlling the corrosion rate of Mg alloys is crucial for the application of Mg alloys. At present, a common way to solve this problem is the surface treatment of Mg alloys [5]. The main technologies include micro-arc oxidation (MAO), chemical conversion treatment, and anodizing, etc.

MAO technology, also known as plasma electrolytic oxidation (PEO), is a method of generating a plasma discharge on the surface of a Mg alloy through the action of a high voltage discharge [6−9]. MAO technology is mature and reliable, with simple equipment and convenient operation. The commonly used electrolytes generally include aluminate [10,11], phosphoric acid [12,13], silicic acid [14,15] and their mixed

Corresponding author: Liang WU, Tel: +86-18983011096, E-mail: wuliang@cqu.edu.cn
DOI: 10.1016/S1003-6326(23)66286-7

systems [16,17]. ZHANG et al [13] demonstrated that under certain conditions, phosphate-based MAO coatings have the best corrosion resistance to Mg alloys. The grown phosphate-based MAO film is uniform and dense, with good adhesion so that the film does not easily fall off, so the MAO film is a good choice for Mg alloy anticorrosion coating. However, the porous structure of MAO coating seriously decreases the corrosion resistance [18]. Corrosive media can easily penetrate the MAO/ substrate interface through the defects, resulting in corrosion at the interface. Therefore, it is necessary to seal the porous MAO coating.

In recent years, metal-organic frameworks (MOFs) have broad application prospects in many fields, such as energy storage, biomedicine, and catalysis, which have attracted the attention of many scientists [8,19]. Current research on MOFs as corrosion inhibitors or protective layers has demonstrated that some MOFs are stable and hydrophobic with potential applications in metal corrosion protection [20,21]. ZIF-67 is composed of cobalt central ions and organic ligands through coordination bonds. As a member of the MOFs family, ZIF-67 is stable in aqueous and strong alkaline solutions, with abundant microporous structure and numerous redox reaction sites, and is considered to be a promising anti-corrosion material [22].

However, the application of MOF coating in the field of anti-corrosion mostly focuses on metals such as carbon steel, aluminum, and copper, and there are not many studies on the corrosion protection of Mg alloys. In addition, the heterogeneous nucleation of MOFs is poor, and the MOF coating cannot completely cover the surface of the metal substrate due to the scattering of grains [23,24]. The insufficient binding force between the MOF coating and the substrate and the limitations of the metal ions in MOFs to the metal substrate also need to be solved urgently.

Based on this, in this study, MAO coatings innovatively grew directly on the AZ31 surface, and a ZIF-67 (a Co-based MOF) was then introduced into the MAO coating to in situ form a MAO/ ZIF-67 composite coating. The objective is to improve the corrosion resistance of AZ31 Mg alloy and the bonding strength of MOFs coating. That is expected to be applied to the anti-corrosion in the all-metal field.

2 Experimental

2.1 Materials

The commercial AZ31 Mg alloy ingot (3−3.2 wt.% Fe, 2.5−3.5 wt.% Al, 0.6−1.3 wt.% Zn, 0.2−1 wt.% Mn, 0.1 wt.% Si, 0.05 wt.% Cu, 0.04 wt.% Ca, balanced Mg) was cut into specimens with dimensions of 18 mm × 18 mm × 5 mm. The specimens were ground with $120^{\#}$−$2000^{\#}$ grit SiC paper in turn and polished, degreased and cleaned for further processing. Anhydrous ethanol, deionized water, trisodium phosphate dodecahydrate ($Na_3PO_4 \cdot 12H_2O$), cobalt(II) nitrate hexahydrate ($Co(NO_3)_2 \cdot 6H_2O$), sodium hydroxide (NaOH), and 2-methylimidazole were all purchased from Shanghai Sinopharm Chemical Reagent Co., Ltd., China. All reagents were analytical reagents and were not further purified. The solvent was deionized water. All reagents and solvents were commercially available and used as provided.

2.2 Preparation of MAO coating

The MAO coating was formed in a system consisting of an electrical signal pulsed AC power source (China) and a polymethyl methacrylate (PMMA) electrolytic cell fitted with stainless steel plates. The anode was AZ31 Mg alloy and the cathode was the stainless steel plates. The electrolyte consisted of $Na_3PO_4 \cdot 12H_2O$ (8.03 g/L) and NaOH (7.14 g/L) and was continuously stirred, and maintained using a water cooling system at (25±5) °C. The frequency was 500 Hz and the duty ratio was 5% (the pulse width was 100 μs). The specimens were washed with deionized water and anhydrous alcohol, and dried in warm air.

2.3 Preparation of MAO/ZIF-67 composite coating

The ZIF-67 (Co-MOF) material was synthesized with slight modifications based on the previous literature [25,26]. A and B solutions were formed by the dissolution of 11.35 g of 2-methylimidazole and 0.54 g of $Co(NO_3)_2 \cdot 6H_2O$ in 100 mL of deionized water. The MAO-coated specimens were placed in the mixed solutions of A and B, at room temperature for 25 h, to prepare the MAO/ZIF-67 composite coating. The cleaning steps for the MAO/ZIF-67 composite coating were the same as above. The preparation process of the composite coating is shown in Fig. 1.

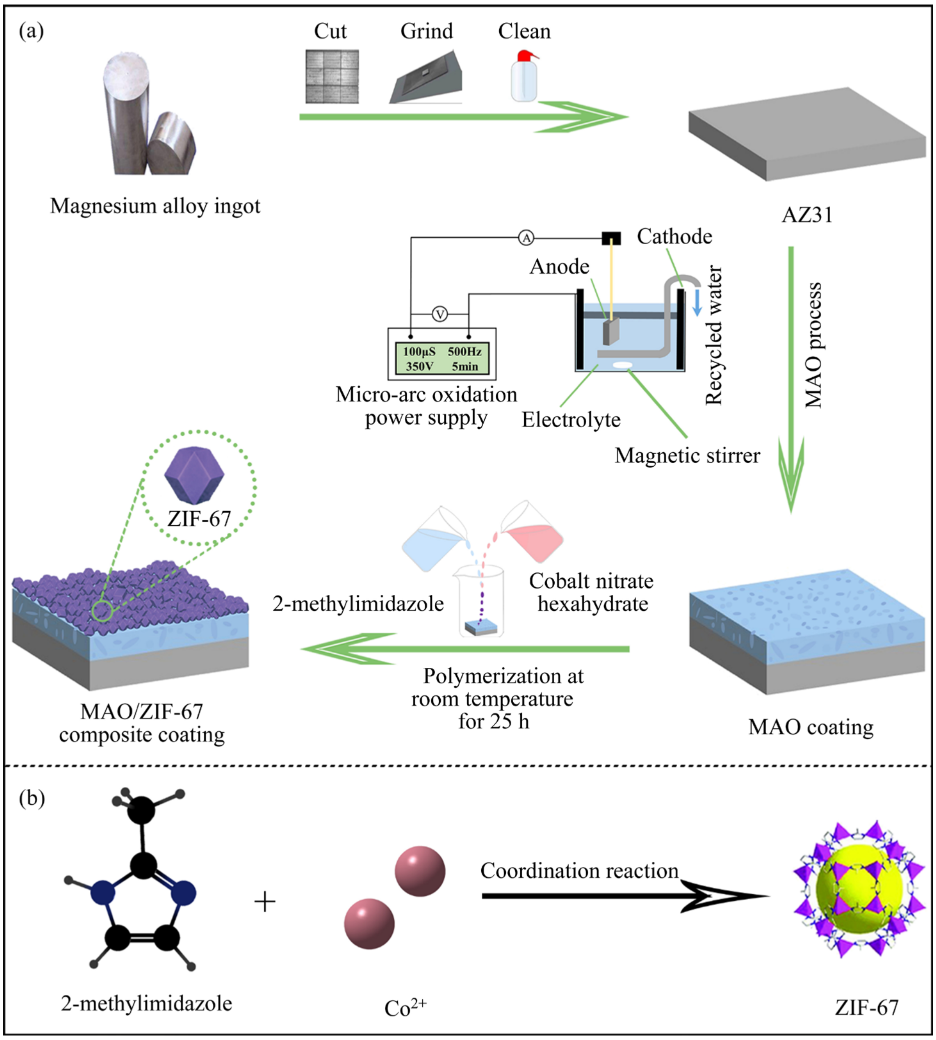

Fig. 1 Preparation process of MAO/ZIF-67 composite coating (a) and schematic diagram of coordination synthesis of ZIF-67 (b)

2.4 Characterization

The surface morphology and cross-sectional thickness of the coatings were investigated using FE-SEM (JSM−7800F, JEOL, field emission scanning electron microscopy, Japan). The elemental composition, chemical state, and molecular crystal structure of the coatings were analyzed using EDS (INCA Energy 350, energy dispersive spectrometer, Oxford, UK), FT-IR (Nicolet IS5, Fourier transform infrared spectra, Thermo Scientific, USA), XRD (D/Max 2500X, X-ray diffraction, Rigaku, Japan) and XPS (ESCALAB 250Xi, X-ray photoelectron spectroscopy, Thermo Scientific, USA). The FT-IR spectra were obtained at infrared wavelengths of 400−4000 cm^{-1}. In the XRD test, a copper target (150 Ma and 40 kV) was used with a scanning angle of 2θ=5°−80°, a scanning rate of 4 (°)/min, and a glancing angle of 1.5°. Metallographic microscope (Zeiss, Germany) was used to evaluate the adhesion between the coating and the Mg substrate.

2.5 Corrosion resistance tests

2.5.1 Electrochemical test

The electrochemical corrosion properties of the alloys were investigated using an electrochemical workstation (Princeton Parstat 4000A, USA). The used corrosion medium was 3.5 wt.% NaCl solution, and the test area was 1 cm^2. The open circuit potential (OCP), electrochemical impedance spectroscopy (EIS) and potential dynamic polarization curves were all measured using a three-electrode system. The saturated calomel electrode was the reference electrode (RE), the platinum electrode was the counter electrode

(CE), and the specimen was the working electrode (WE). Potential dynamic polarization curves from the cathode to the anode were obtained in the OCP range from −0.5 to 0.5 V at a scan rate of 2 mV/s. EIS was measured in the frequency range from 10 mHz to 100 kHz using a 10 mV sinusoidal signal. The ZsimpWin software was used to fit the equivalent circuits. The corrosion current density (J_{corr}) and corrosion potential (φ_{corr}) were obtained by fitting the dynamic potential polarization curves using Tafel extrapolation.

2.5.2 Hydrogen evolution test

The hydrogen evolution experiments were carried out with a simple homemade device as the previous literature [27]. The entire surface of the specimen was exposed to 3.5 wt.% NaCl solution and the evolved hydrogen was collected in a burette channeled using inverted funnels. The hydrogen evolution volume (HEV, mL/cm^2) was recorded every 12 h. The HER (hydrogen evolution rate, mL/(cm^2·h) was evaluated based on the average of each HEV. This step continued until the solution in the burettes was discharged. The optical morphology of the specimens after the hydrogen evolution experiment was recorded using a digital camera.

2.6 Scratch test

The adhesion was determined according to the national standard GB/T 9286—1998. A QFH type 100-grid knife was used to cut a cross-lattice pattern on the MAO/ZIF-67 composite coating surface. The incision reached the substrate. Then, the surface was cleaned with a brush five times diagonally across the 100-grid knife, and a tape was used to stick to the incision and to pull it apart. Finally, the lattice area was examined with a magnifying glass, and the surface morphology of the coating was characterized with a metallographic microscope and a SEM to assess the adhesion between the MAO/ZIF-67 composite coating and the AZ31 substrate.

3 Results and discussion

3.1 Structure and composition

The successful synthesis of MAO/ZIF-67 composite coating was confirmed by the structural analysis using SEM−EDS, FT-IR, XRD and XPS. The morphologies of the AZ31 substrate, the MAO coating and the MAO/ZIF-67 composite coating are displayed in Fig. 2. Corrosion susceptibility is jointly determined by the overall properties and can be evaluated from the surface uniformity, compactness, chemical composition, phase structure and coating thickness of the coating, including micro cracks and micro-pores in the coating [28−31]. Figures 2(a, b) present the bare AZ31 substrate after grinding without any treatment at low and moderate magnifications. Compared with the AZ31 substrate, the surface of the MAO ceramic coating (Figs. 2(c, d)) is composed of many melts of different sizes, uniformly distributed, with pores on the top, which are shaped like a “volcano”. This surface defect is caused by MAO process. During the breakdown of the MAO discharge, the surface of the coating is in contact with the electrolyte. The melt rapidly solidifies and releases gas, resulting in the volcano shapes. Figures 2(e, f) present the composite coating obtained by the MAO pretreatment. ZIF-67 nucleated well, formed a continuous coating completely covering the MAO surface, and achieved the sealing effect, corresponding to the work of others [32]. The MAO/ZIF-67 composite coating is dense, with few pores and no obvious micro-cracks. The composite coating has fewer surface defects than the MAO coating and the surface of the MAO coating has been sealed. Different surface morphologies illustrate the MAO and MAO/MOF composite coatings.

The contents of elements for each specimen measured by EDS are listed in Table 1. P is presented in the MAO coating, and Co is presented in the MAO/ZIF-67 composite coating, implying the successful growth of the coating. The growth of the coating is accompanied by the decrease of the Mg content and the increase of the C content. C may come from CO_2 in the air; however, the MOF itself can capture CO_2 [33], which makes the C content in the composite coating higher than that in the MAO. It is indicated that the MAO coating is covered by the MAO/ZIF-67 composite coating. Furthermore, Fig. 2(f) indicates that ZIF-67 exhibits a rhombic dodecahedron polyhedral structure with a size below 1 μm. The surface of each rhombus is smooth, and the symmetry is high, indicating that the synthesized ZIF-67 has good crystallinity, consistent with literature results [22,34]. Therefore, the method in this study could be used to successfully prepared well-structured ZIF-67.

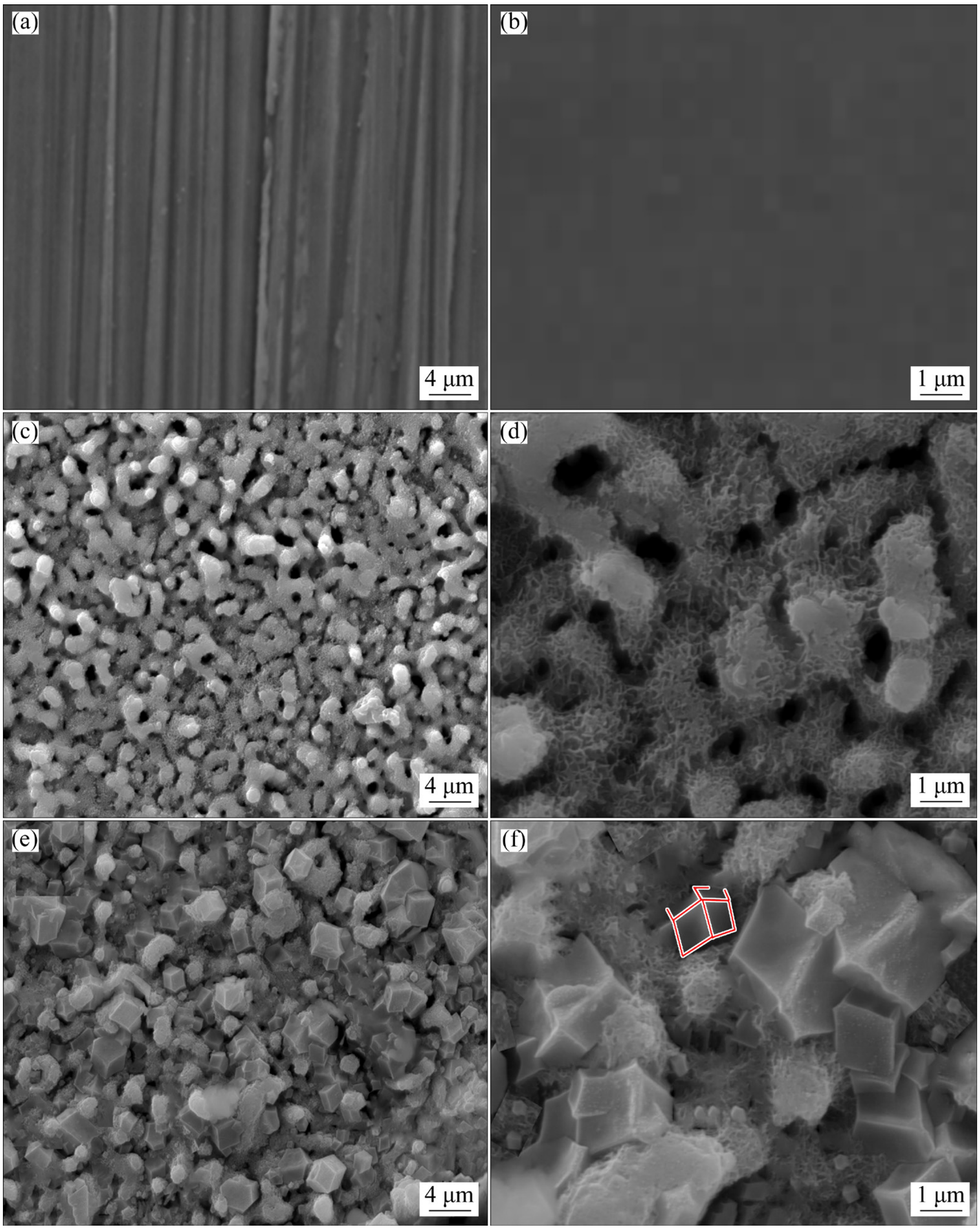

Fig. 2 SEM images for AZ31 substrate (a, b), MAO coating (c, d) and MAO/ZIF-67 composite coating (e, f)

Table 1 Contents of elements in each specimen detected by EDS

Specimen	Content/at.%						
	Mg	C	O	Al	P	N	Co
AZ31	89	7	3	1			
MAO	40	21	22	1	16		
MAO/ZIF-67	16	46	18	2	5	10	3

Figure 3 presents the cross-sectional views of MAO coating (Fig. 3(a)) and MAO/ZIF-67 composite coating (Fig. 3(b)). The maps of the corresponding elements and contents are arranged after the cross-sectional views. The cross-sectional morphology shows a uniform coating that completely covers the AZ31 substrate that can be a barrier layer for the corrosive media. The MAO coating thickness is about 3.28 μm and is porous. The MAO/ZIF-67 composite coating thickness is about 4.11 μm. The two different coatings contain two representative elements, P and Co, which indicates the growth positions of the coatings.

The formation of functional groups and coordination polymers on the MAO/ZIF-67 composite coating is identified using FT-IR (Fig. 4(a)). Each absorption peak in the spectrum is matched with the corresponding vibration. The characteristic peaks at approximately 2922 cm^{-1} (3000−2800 cm^{-1}) and 3132 cm^{-1} (3200−3100 cm^{-1}) are attributed to the stretching of aliphatic and aromatic C—H bonds in 2-methylimidazole. The peaks at 1450−1400 cm^{-1} are attributed to C═O vibrations. The absorption peak at 1417 cm^{-1} corresponds to the stretching vibration of the C═N double bonds, and the bands at 1400−600 cm^{-1} are attributed to the stretching

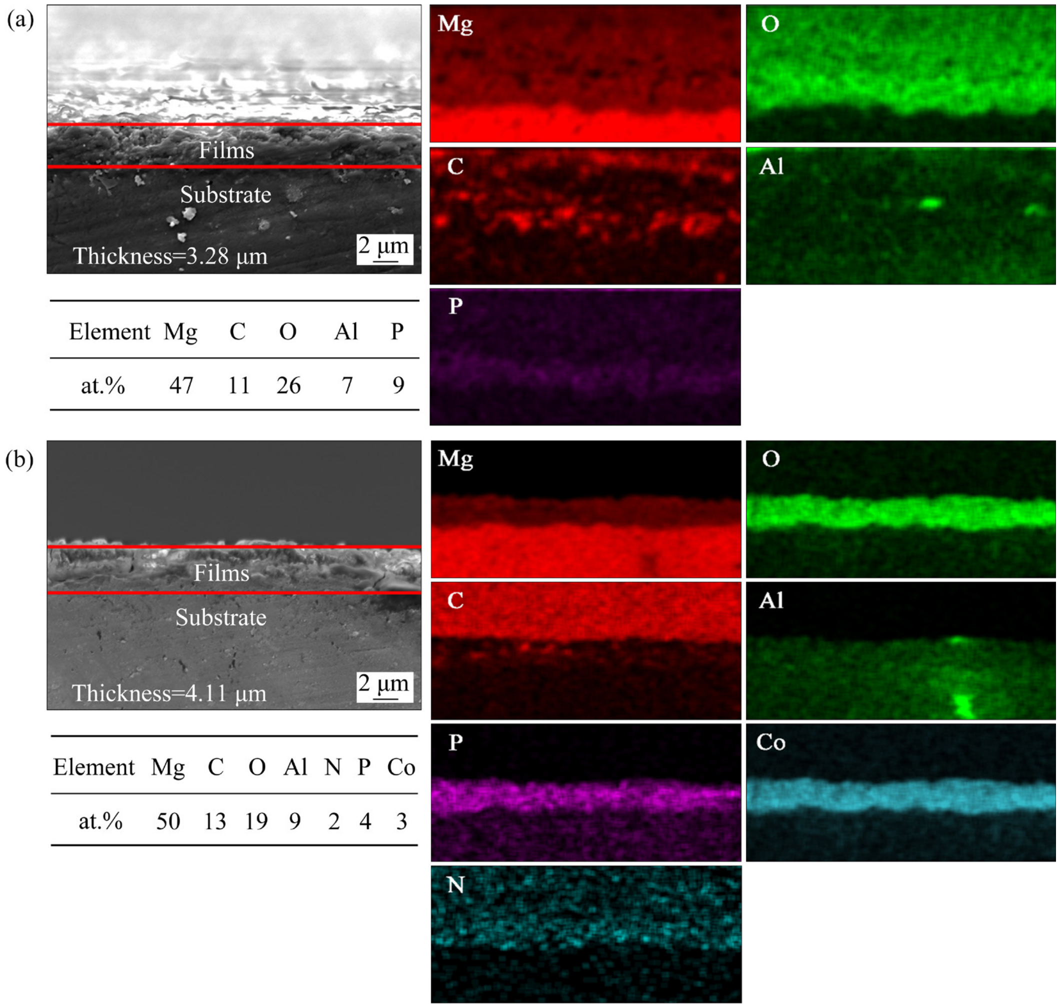

Element	Mg	C	O	Al	P
at.%	47	11	26	7	9

Element	Mg	C	O	Al	N	P	Co
at.%	50	13	19	9	2	4	3

Fig. 3 Cross-sectional morphologies and corresponding EDS maps of MAO coating (a) and MAO/ZIF-67 composite coating (b)

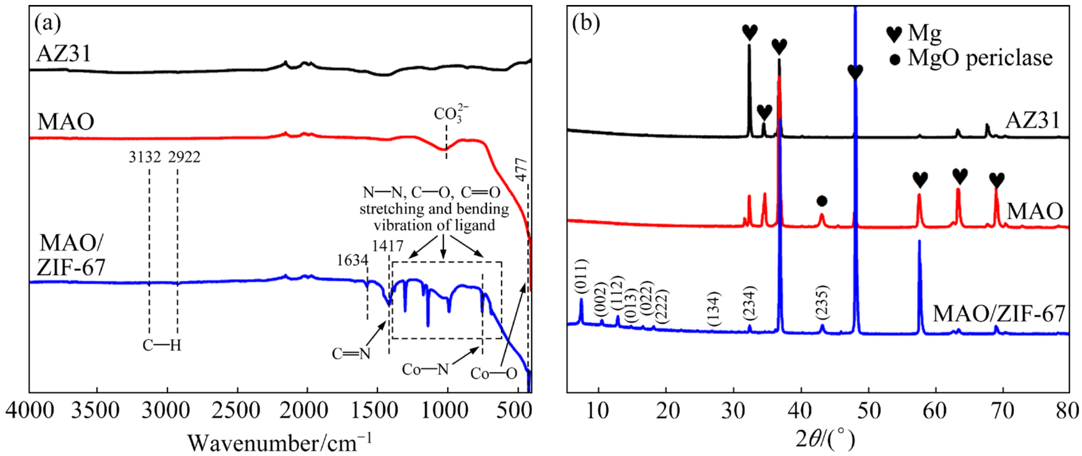

Fig. 4 FT-IR spectra (a) and XRD patterns (b) of AZ31, MAO coating and MAO/ZIF-67 composite coating

vibrations of N—H and C—O, as well as the bending and stretching vibrations of the imidazole ring [25,35]. The stretching vibration of N—H indicates that hydrogen bonding is involved in the complex formation [22]. As a result, ZIF-67 nanoparticles can be stably grown in situ on the surface of MAO coating. The peak at 750.5 cm^{-1} is Co—N bond vibration. The bands between 900 and 1350 cm^{-1} originate from the in-plane bending of the imidazole ring (ligand). The peak at 500−800 cm^{-1} is caused by the out-of-plane bending of the imidazole ring [25]. A new characteristic peak at 477 cm^{-1} in the MAO/ZIF-67 is assigned to the stretching vibration of the Co—O bonds. In addition, the blue transition occurs at a wavenumber of 1634 cm^{-1}, inferring the interaction of Co^{2+}. The results of infrared spectra indicate that the as-prepared MAO/ZIF-67 composite coating is formed by the coordination of 2-methylimidazole with the central cobalt ion.

To investigate the phase composition and structural information of the synthesized MAO/ZIF-67 composite coating, the specimens were characterized using XRD. Figure 4(b) shows that the diffraction peaks of Mg (2θ=30°−40°) in the MAO coating are weaker than those in AZ31, probably because of the thicker ceramic film. There are peaks for magnesium oxide (MgO) in the spectrum. The strongest diffraction peaks (2θ=30°−40°) of Mg in the MAO/ZIF-67 composite coating decrease, due to the increased thickness of the coating, which is also consistent with the results in the cross-sectional images in Fig. 3. The MAO/ZIF-67 composite coating has characteristic diffraction peaks, corresponding to the crystal planes: 7.31° (011), 10.36° (002), 12.72° (112), 14.40° (013), 16.45° (022), 18.04° (222), 26.70° (134), 32.53° (234) and 43° (235) [25], which is in good agreement with the characteristic peak positions of standard XRD data. The central cobalt ion is surrounded by an imidazole network, indicating the successful preparation of ZIF-67 coating with high crystallinity on the MAO coating [36].

To further elucidate the chemical composition and element valence states of the ZIF-67, XPS analysis was performed on the MAO/ZIF-67 composite coating. Figure 5(a) presents the full spectrum of the composite coating, and the peaks of Mg 1s, Co 2p, O 1s, N 1s and C 1s. Figure 5(b) shows that Mg is in the form of MgO, $Mg(OH)_2$ and Mg. The presence of MgO is consistent with the XRD patterns. The narrow-scan XPS spectrum of Co 2p (Fig. 5(c)) indicates several main peaks at 780.7, 782 and 796.3, 798 eV corresponding to Co $2p_{3/2}$ and Co $2p_{1/2}$, respectively. The satellite peaks of Co $2p_{3/2}$ (Sat.) and Co $2p_{1/2}$ (Sat.) are located around 786.8, 789.1 and 802.6, 805.5 eV, which are attributed to the Co $2p_{3/2}$ and Co $2p_{1/2}$ binding energy, respectively. Co(II) is the predominant form in the ZIF-67 coating. Figure 5(d) shows that the two main peaks are detected at 531.3 and 531.9 eV, corresponding to CO_3^{2-} and O—C═C, respectively. There is also a characteristic peak at 529.5 eV, which indicates Co—O bonds [37]. Since the coating is prepared with 2-methylimidazole as the ligand, the coating contains N and C. The N 1s high-resolution spectrum (Fig. 5(e)) indicates the N—O bonds and N—H bonds. Likewise, there are C═O, C═N, C—C/C═C, C—O and C—H bonds in the C 1s spectrum (Fig. 5(f)). The XPS results indicate that 2-methylimidazole and Co^{2+} ions are present in the MAO/ZIF-67 composite coating. At the same time, it is also shown that the binding force between ZIF-67 nanoparticles and MAO film is realized by hydrogen bonding, which is consistent with the FT-IR results.

3.2 Corrosion resistance

3.2.1 Polarization curves

Figure 6 presents the dynamic polarization curves of different specimens in 3.5 wt.% NaCl solution. A point of intersection is obtained by extrapolating along the tangent of the cathodic and anodic polarization curves. The corresponding vertical axis is the corrosion potential, and the horizontal axis is the corrosion current density. The corresponding corrosion current density (J_{corr}), corrosion potential (φ_{corr}), anodic Tafel slope (b_a) and cathodic Tafel slope (b_c) of each specimen are listed in Table 2. The magnitude of J_{corr} directly reflects the corrosion resistance of materials in corrosive media. The corrosion potential represents the ability for corrosion, but is not related to the corrosion rate. The corrosion current density is related to the speed of corrosion. The corrosion resistance of coatings cannot be measured in terms of φ_{corr}. However, a lower corrosion density (J_{corr}) indicates a lower corrosion rate [38,39]. Table 2

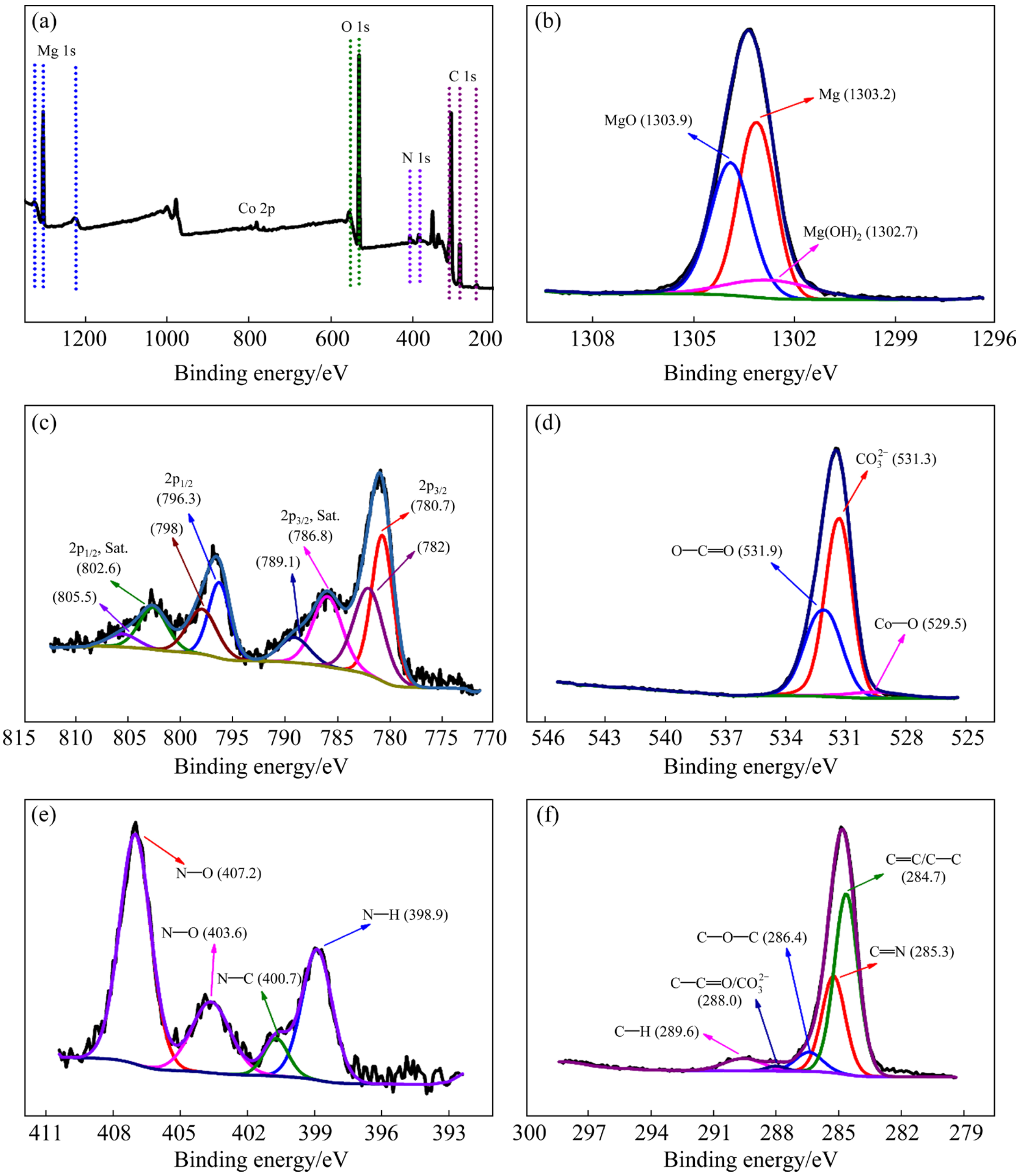

Fig. 5 Full XPS spectrum of MAO/ZIF-67 composite coating (a) and narrow scan spectra of elements for Mg 1s (b), Co 2p (c), O 1s (d), N 1s (e) and C 1s (f)

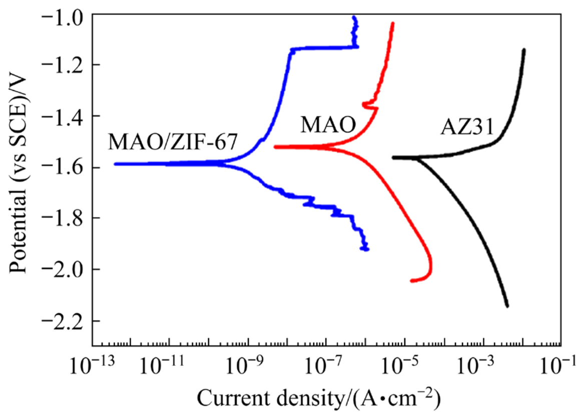

Fig. 6 Dynamic potential polarization curves of different specimens tested in 3.5 wt.% NaCl solution

indicates that φ_{corr} of the AZ31 substrate is −1.56 V, and J_{corr} is 3.1×10^{-5} A/cm^2. The MAO coating has φ_{corr} positively shifted by 50 mV to −1.51 V, and J_{corr} is 4.1×10^{-7} A/cm^2. The MAO/ZIF-67 composite coating has φ_{corr} of −1.59 V, and J_{corr} is 7.8×10^{-8} A/cm^2, which is 3 orders of magnitude lower than that of the AZ31 substrate. The improved corrosion performance of MAO/ZIF-67 coatings may be attributed to the uniform distribution of ZIF-67 on the MAO film, which hinders the solution from reaching the AZ31 alloy matrix. The corrosion kinetics is reduced, the corrosion rate is greatly reduced, and the corrosion resistance is significantly improved. Therefore, ZIF-67 coating has broad application prospects as an anti-corrosion coating.

3.2.2 Electrochemistry impedance spectrum

Using a small amplitude sine wave potential as a disturbance signal, the electrode system produced an approximate linear response, and the impedance spectrum of the electrode system was measured in a wide range [40]. The method used to study the electrode system is EIS. The real and imaginary parts of the impedance are presented by the Nyquist plot (Fig. 7(a)). The EIS data corresponding to the coatings present two arc-shaped capacitances, indicating that the electrode reaction at this potential is controlled by activation. The electrode system has two time constants. Moreover, the centers of the two capacitance arcs are deflected below the real axis, showing an “dispersion effect”, which may be related to the inhomogeneity of the electrode/electrolyte interface [11]. The corrosion rate of the coatings can be estimated from the radius of the arcs, the radius of the capacitive arc of AZ31 is smaller, and the radius of the MAO is larger. This indicates that neutral solution has a corrosive effect on the coating, but does not completely destroy the oxide film. The capacitance arc of the MAO/ZIF-67 composite coating is the largest, indicating that the oxide film is denser, has a strong protective effect on the Mg alloy matrix, and has a lower corrosion rate. This result is consistent with the polarization curves, indicating that the two techniques show similar trends in corrosion rate.

The Bode plot and the phase angle (Figs. 7(b, c)) show the corrosion behavior of the coatings in neutral media, in agreement with the Nyquist plot in Fig. 7(a). 10^2−10^5 Hz is a high frequency range, reflecting the characteristics of the outer layer, 10^0−10^2 Hz is a medium frequency

Table 2 Polarization curve parameters obtained from AZ31 and coatings

Specimens	φ_{corr} (vs SCE)/V	J_{corr}/(A·cm^{-2})	b_c/(mV·dec^{-1})	b_a/(mV·dec^{-1})
AZ31	−1.56±0.06	(3.1±0.3)×10^{-5}	198±9	29±13
MAO	−1.51±0.15	(4.1±1.4)×10^{-7}	145±7	148±17
MAO/ZIF-67	−1.59±0.13	(7.8±0.5)×10^{-8}	110±11	242±9

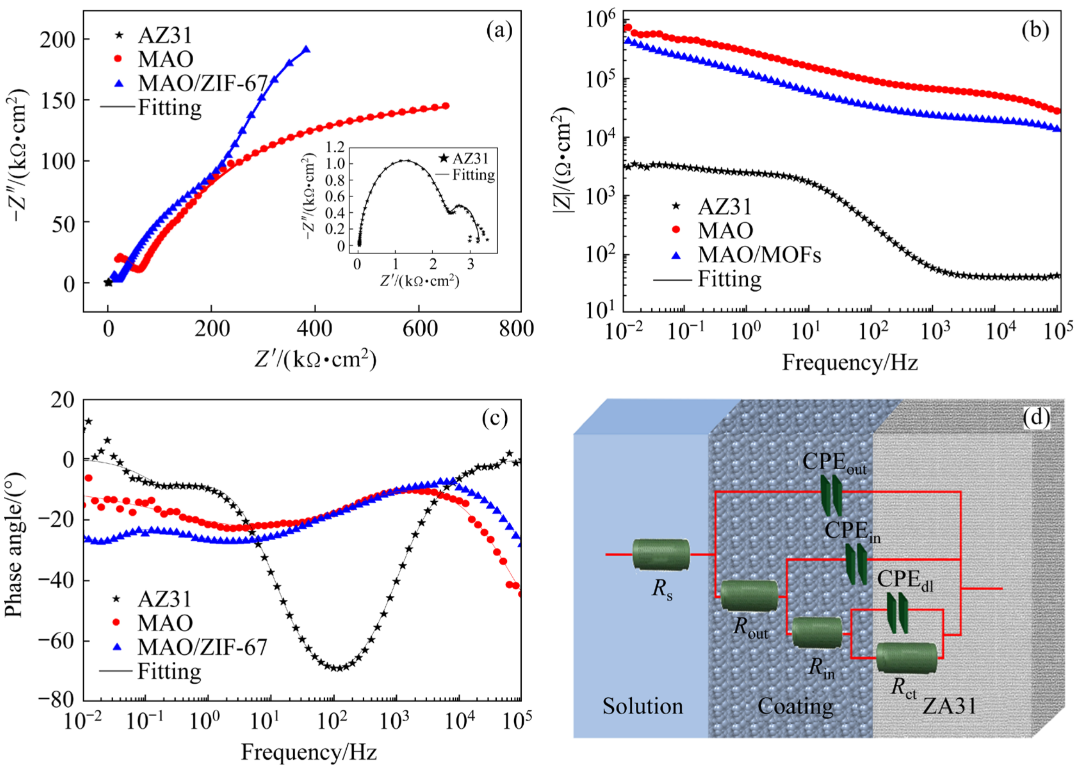

Fig. 7 EIS data and fitting curves for different specimens (a−c) and applicable equivalent circuit model fitted to EIS spectra (d)

range, reflecting the characteristics of the inner layer, and less than 10^0 Hz is a low frequency range, reflecting the interface of the substrate and coating. The $|Z|$ value of the MAO/ZIF-67 composite coating is the largest, indicating that the coating has the lowest corrosion rate. At high frequency, the phase angle of MAO/ZIF-67 composite coating is larger than that of MAO coating, which indicates that the MAO/ZIF-67 composite coating in attenuating the corrosion process is better than that of MAO coating.

The electrochemical performance of the coatings was modelled using the EC (equivalent circuit). The EC (Fig. 7(d)) was fitted to EIS with a Chi-square value (χ^2) less than or equal to 1×10^{-3}. The existence of "dispersion effect" indicates that the electric-double layer at the electrode interface cannot be equivalent to a pure ideal capacitor, and is described by a constant phase angle element with capacitive properties. This constant phase angle element is represented by the symbol CPE. CPE has two parameters: one is Y_0 whose dimension is $\Omega^{-1}\cdot cm^{-2}\cdot s^n$, the other is n ($0<n<1$), a dimensionless index, sometimes called the "dispersion index". In addition, R_{in} and CPE_{in} are the resistance response and capacitance of the inner dense layer, respectively. R_{out} and CPE_{out} represent the resistance response and capacitance of the outer void layer, respectively. The capacitance of the substrate−electrolyte response interface is denoted by CPE_{dl}. R_s is related to the solution resistance, corresponding to the intersection of the semicircle and the X-axis in the Nyquist plot [38].

The parameters of each equivalent element obtained by fitting are presented in Table 3. The electrochemical parameter (R_{ct}) for MAO/ZIF-67 composite coating indicates the speed of the charge transfer reaction. The magnitude of the charge transfer resistance R_{ct} (the radius of the semicircle in Fig. 7(a)) of the electrochemical reaction at the interface between the solution and the coating is the main parameter for evaluating the corrosion rate of the coatings. In general, the corrosion rate is inversely proportional to the R_{ct} value. The larger the R_{ct} value, the lower the corrosion rate [41]. In NaCl solution, the EIS analysis indicates that different oxide films have different corrosion rates. Compared with other coatings, the R_{in} ($2.6\times10^6\ \Omega\cdot cm^2$) and R_{out} ($1.5\times10^5\ \Omega\cdot cm^2$) values of MAO/ZIF-67 composite coating are the largest, the CPE_{in} (2.8×10^{-7}) and CPE_{out} (4.8×10^{-10}) are the smallest. This may be due to the coverage of the MOFs coating. The exposed electrode surface area is reduced and the double film thickness is increased, effectively delaying the corrosion process of ion diffusion from the electrolyte to the electrode interface, and significantly improving the corrosion resistance. In conclusion, the MAO/ZIF-67 composite coating has the lowest permeability of corrosive medium through the coating pores, and the lowest corrosion rate.

3.2.3 Hydrogen evolution

After the hydrogen evolution experiment, the surface appearance of the specimens was recorded. After immersion for 300 h, the corrosion of AZ31 substrate, MAO coating, and MAO/ZIF-67 composite coating all started from the edge and showed significant corrosion products (Fig. 8). Nevertheless, the MAO/ZIF-67 composite coating reflects a partially intact surface and only localized corrosion at corners. This further indicates that the introduction of ZIF-67 metal-organic framework into the surface of the Mg alloy MAO anti-corrosion coating effectively delays the penetration of corrosion ions into the alloy surface and increases the integrity of the composite coating. In addition, the experimental results of different specimens immersed in 3.5 wt.% NaCl solution at room temperature are shown in Fig. 9, i.e. the HEV (Fig. 9(a)), and the HER (Fig. 9(b)). The total hydrogen volume evolved from each specimen increases with prolonging immersion time. AZ31

Table 3 Electrochemical parameters of specimens obtained from fitting EIS data

Specimen	CPE_{out}		R_{out}/ ($\Omega\cdot cm^2$)	CPE_{in}		R_{in}/ ($\Omega\cdot cm^2$)	CPE_{dl}		R_{ct}/ ($\Omega\cdot cm^2$)	χ^2
	Y_0/ ($\Omega^{-1}\cdot cm^{-2}\cdot s^n$)	n		Y_0/ ($\Omega^{-1}\cdot cm^{-2}\cdot s^n$)	n		Y_0/ ($\Omega^{-1}\cdot cm^{-2}\cdot s^n$)	n		
AZ31	9.5×10^{-7}	0.7	2.5×10^4	4.0×10^{-4}	0.7	1.3×10^5				3.4×10^{-3}
MAO	4.8×10^{-10}	0.9	1.3×10^5	3.4×10^{-6}	0.4	0.7×10^6	2.6×10^{-4}	1	2.8×10^5	4.8×10^{-3}
MAO/ZIF-67	4.8×10^{-10}	0.9	1.5×10^5	2.8×10^{-7}	0.4	2.6×10^6	5.1×10^{-5}	0.9	4.6×10^5	2.2×10^{-3}

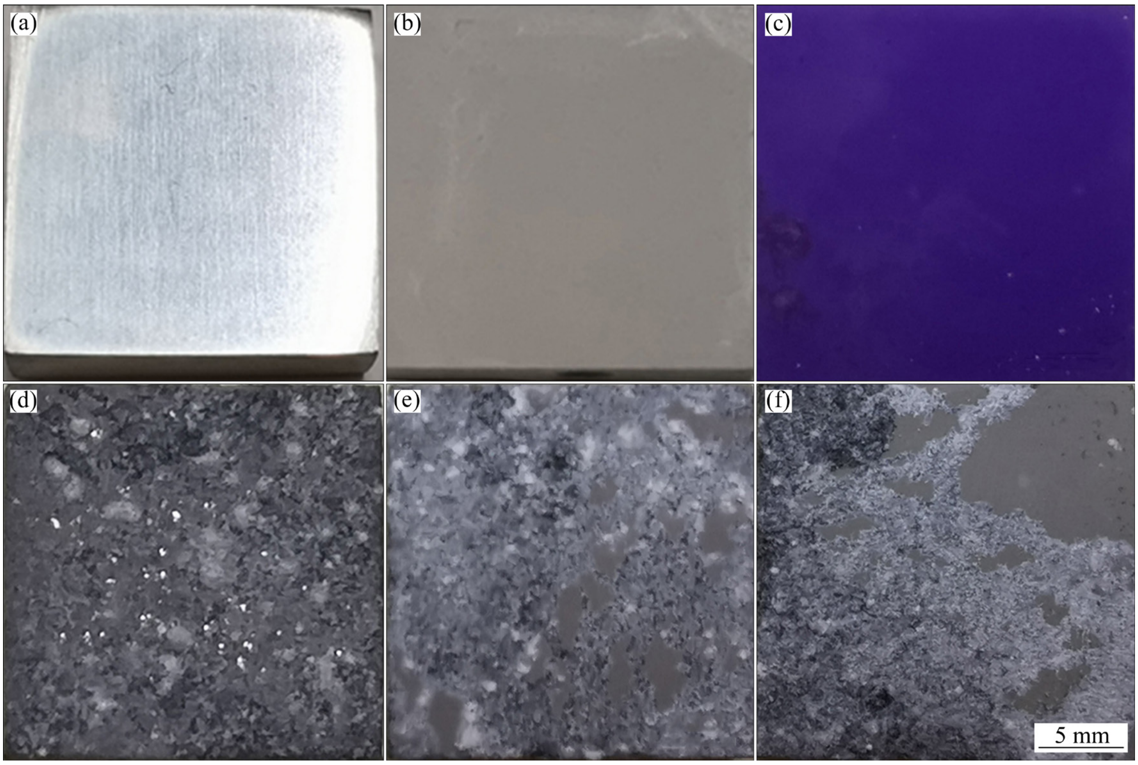

Fig. 8 Comparison of surface morphologies of different specimens: (a−c) Morphologies of AZ31, MAO, and MAO/ZIF-67 before hydrogen evolution experiment, respectively; (d−f) Corresponding specimens after hydrogen evolution experiment

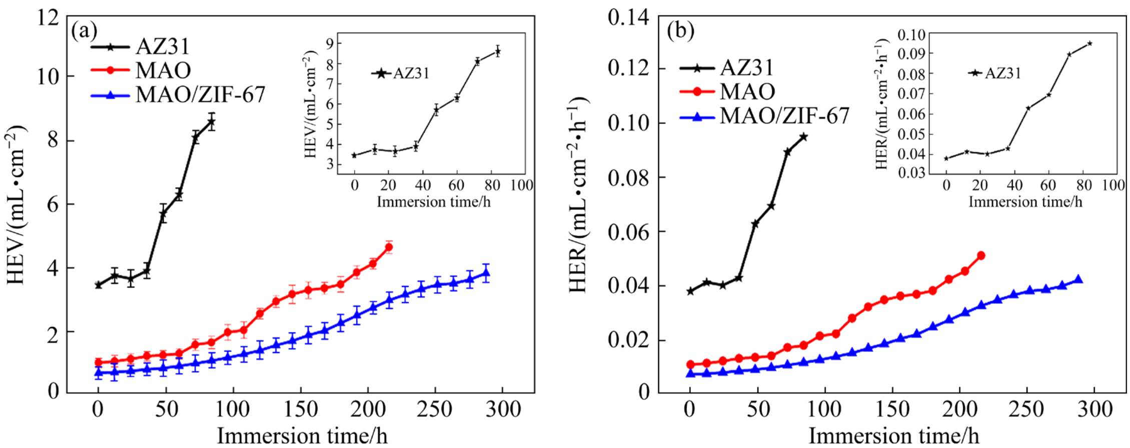

Fig. 9 HEV (a) and HER (b) of different specimens in 3.5 wt.% NaCl solution

exhibits significantly more hydrogen evolution of 8.60 mL/cm^2 within 100 h of immersion, with an average HER of 0.50 mL/(cm^2·h). The hydrogenation effect of the MAO coating and the MAO/ZIF-67 composite coating is small. The HEV of MAO coating within 230 h is 4.64 mL/cm^2, the HER is 0.22 mL/(cm^2·h). The MAO/MOFs composite coating has lower HEV (3.82 mL/cm^2) and HER (0.16 mL/(cm^2·h)) within 300 h, further indicating that the coating has a good protective effect on the AZ31 substrate, proving that the coating provided good corrosion resistance. This is consistent with the EIS results.

3.3 Scratch adhesion

The adhesion strength between the metal matrix and coating is an important factor that determines the reliability and service life of coating. As an anticorrosion coating for metal substrates, since MAO coating has good adhesion, the adhesion of the MAO/ZIF-67 coating is also expected to be good. The damage of the coating is mainly caused by plastic deformation [42]. According to the adhesion classification specified in ISO 2409:2013 [43], the ZIF-67 film has an adhesion grade of 1, with a small part falling off at higher load (Figs. 10(c, d)), but the edges at the intersection of the incisions are clear and smooth without obvious falling off (Figs. 10(a, b)). This can characterize the cohesive strength inside the coating, which also proves that the prepared MAO/ZIF-67 composite coating can be used as a high-strength and good-quality anti-corrosion coating.

3.4 Corrosion resistance mechanism

Figure 11 depicts the schematic diagrams of the mechanism corrosion protection of the as-prepared MAO coating and MAO/ZIF-67 composite coating with the AZ31 substrate as a comparison. The exposed AZ31 alloy can spontaneously undergo corrosion in a humid environment, forming an unstable oxide film [44], as shown in Fig. 11(a). The corrosive media (such as water, O_2 and Cl^-) can easily destroy this unstable oxide film and reach the surface of the alloy, thereby corroding the Mg alloy. In Fig. 11(b), the Mg alloy substrate is treated with MAO to form a MAO coating, which can provide corrosion protection for the substrate. However, the MAO coating has many defects such as micro-cracks and pores, and the corrosive medium can easily infiltrate into the metal interface through pores and cracks, and then corrode the MAO coating. For the MAO/ZIF-67 composite coating system, the anticorrosion mechanism may be the in-situ growth of a large number of ZIF-67 crystals on the MAO surface to fill the voids of MAO, form a dense coating, protect against penetration of corrosive media, and provide a protective effect for the AZ31 alloy [45,46], acting as a barrier layer and improving the barrier properties of the composite coating (Fig. 11(c)). In addition, the SEM results show that ZIF-67 is a rhombic dodecahedron, and the ZIF-67 coating formed by stacking increases the tortuous conduction path of corrosive media and endows the MAO/ZIF-67 composite coating with a labyrinth effect. When the MAO/ZIF-67 composite coating is damaged due to accidental scratching, corrosive medium such as Cl^- can diffuse into the damaged coating, dissolve the matrix to form Mg^{2+}, and generate a large amount of OH^-. Mg^{2+}, Co^{2+} and 2-methylimidazole molecules can chemically react with OH^-. The reaction products are adsorbed in the anode area, again hindering the intrusion of the corrosive medium. In short, the MAO/ZIF-67 composite coating shows good anticorrosion properties, mainly due to the good growth of ZIF-67 on the MAO coating.

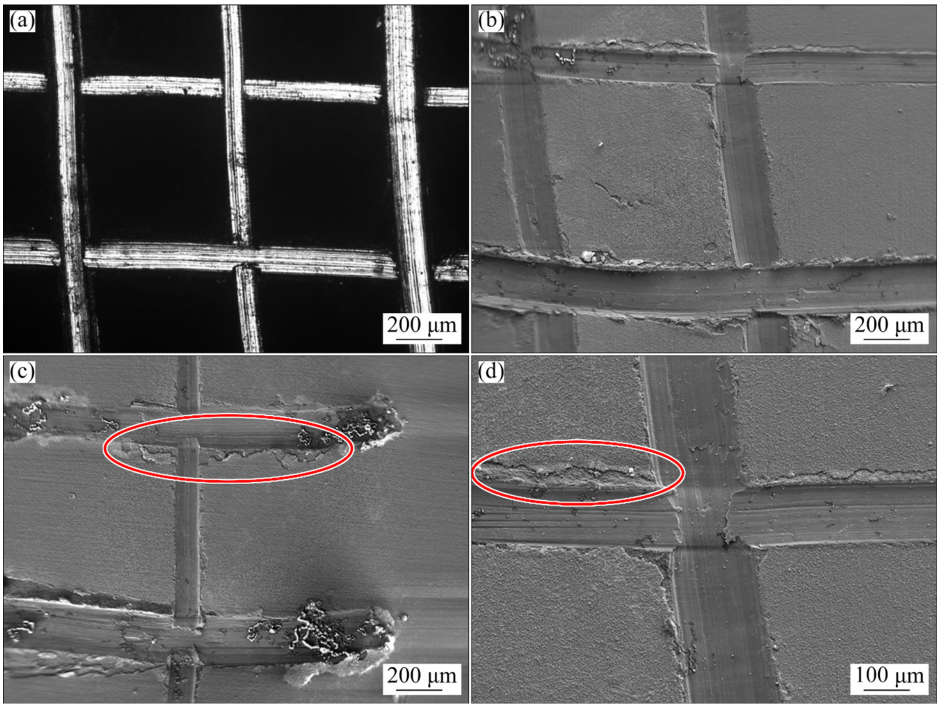

Fig. 10 Metallographic micrograph (a) and SEM images (b−d) of scratches on MAO/ZIF-67 composite coating

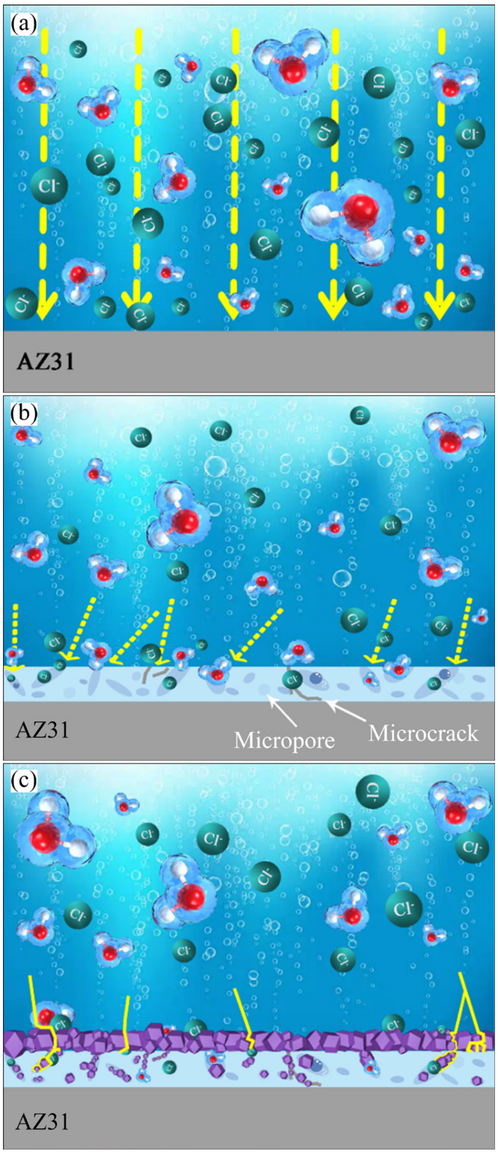

Fig. 11 Schematic diagrams of corrosion mechanism of different specimens: (a) AZ31 substrate; (b) MAO coating; (c) MAO/ZIF-67 composite coating

4 Conclusions

(1) The ZIF-67 nanoparticles synthesized from Co^{2+} and 2-methylimidazole have good crystallinity and a rhombic dodecahedron structure.

(2) The ZIF-67 nanoparticles can effectively seal the micro-pores of the MAO coating, enabling the MAO/ZIF-67 composite coating to achieve the desired density. The dense composite coating significantly improves the corrosion resistance of Mg alloys in 3.5 wt.% NaCl solution.

(3) MAO pretreatment increases the binding force between MOFs and the substrate. The good adhesion further ensures the effective sealing of the MAO micro-pores by the ZIF-67 particles, which makes the composite coating structure more compact, has better barrier properties to corrosive ions, effectively protects the magnesium matrix, and achieves high-quality anticorrosion.

(4) The MAO pretreatment-assisted preparation method is universal and can realize the construction of MOFs coatings on various metal surfaces, expanding the application of MOFs materials in the field of metal corrosion protection.

Acknowledgments

This work was supported by the National Natural Science Foundation of China (Nos. 51971040, 52171101, 52001036, 51971044), the Natural Science Foundation of Chongqing, China (No. cstc2021jcyj-msxmX0613), and the Independent Research Project of State Key Laboratory of Mechanical Transmissions, China (No. SKLMT-ZZKT-2022M12).

References

[1] YIN Zheng-zheng, QI Wen-chen, ZENG Rong-chang, CHEN Xiao-bo, GU Chang-dong, GUAN Shao-kang, ZHENG Yu-feng. Advances in coatings on biodegradable magnesium alloys [J]. Journal of Magnesium and Alloys, 2020, 8: 42−65.

[2] ATRENS A, SONG Guang-ling, CAO Fu-yong, SHI Zhi-ming, BOWEN P K. Advances in Mg corrosion and research suggestions [J]. Journal of Magnesium and Alloys, 2013, 1: 177−200.

[3] ATRENS A, SONG Guang-ling, LIU Ming, SHI Zhi-ming, CAO Fu-yong, DARGUSCH M S. Review of recent developments in the field of magnesium corrosion [J]. Advanced Engineering Materials, 2015, 17: 400−453.

[4] LI Yang, SHI Zhi-ming, CHEN Xing-rui, ATRENS A. Anodic hydrogen evolution on Mg [J]. Journal of Magnesium and Alloys, 2021, 9: 2049−2062.

[5] MA Xiao-chun, JIN Si-yuan, WU Rui-zhi, WANG Jia-xiu, WANG Gui-xiang, KRIT B, BETSOFEN S. Corrosion behavior of Mg−Li alloys: A review [J]. Transactions of Nonferrous Metals Society of China, 2021, 31: 3228−3254.

[6] AZARIAN N, MOUSAVI K S M. Characteristics of a multi-component MgO-based bioceramic coating synthesized in-situ by plasma electrolytic oxidation [J]. Journal of Magnesium and Alloys, 2021, 9: 1595−1608.

[7] MOLAEI M, BABAEI K, FATTAH-ALHOSSEINI A. Improving the wear resistance of plasma electrolytic oxidation (PEO) coatings applied on Mg and its alloys under the addition of nano- and micro-sized additives into the electrolytes: A review [J]. Journal of Magnesium and Alloys, 2021, 9: 1164−1186.

[8] WEI Bing-jian, CHENG Yu-lin, LIU Yuan-yuan, ZHU Zhun-da, CHENG Ying-liang. Corrosion and wear resistance of AZ31 Mg alloy treated by duplex process of magnetron

sputtering and plasma electrolytic oxidation [J]. Transactions of Nonferrous Metals Society of China, 2021, 31: 2287−2306.

[9] DAVOODI F, ATAPOUR M, BLAWERT C, ZHELUDKEVICH M. Wear and corrosion behavior of clay containing coating on AM 50 magnesium alloy produced by aluminate-based plasma electrolytic oxidation [J]. Transactions of Nonferrous Metals Society of China, 2021, 31: 3719−3738.

[10] ZHANG Gen, WU Liang, TANG Ai-tao, MA Yan-long, SONG Guang-Ling, ZHENG Da-jiang, JIANG Bin, ATRENS A, PAN Fu-sheng. Active corrosion protection by a smart coating based on a MgAl-layered double hydroxide on a cerium-modified plasma electrolytic oxidation coating on Mg alloy AZ31 [J]. Corrosion Science, 2018, 139: 370−382.

[11] CHEN Yan-ning, WU Liang, YAO Wen-hui, CHEN Yong-hua, ZHONG Zhi-yong, CI Wen-jun, WU Jia-hao, XIE Zhi-hui, YUAN Yuan, PAN Fu-sheng. A self-healing corrosion protection coating with graphene oxide carrying 8-hydroxyquinoline doped in layered double hydroxide on a micro-arc oxidation coating [J]. Corrosion Science, 2022, 194: 109941.

[12] ROKOSZ K, HRYNIEWICZ T, GAIASCHI S, CHAPON P, RAAEN S, MALORNY W, MAT S D, PIETRZAK K. Development of porous coatings enriched with magnesium and zinc obtained by DC plasma electrolytic oxidation [J]. Micromachines, 2018, 9: 332.

[13] ZHANG Gen, JIANG E, WU Liang, TANG Ai-tao, ATRENS A, PAN Fu-sheng. Active corrosion protection of phosphate loaded PEO/LDHs composite coatings: SIET study [J]. Journal of Magnesium and Alloys, 2022, 10: 1351−1357.

[14] WU Ming-jin, JIANG Feng. Effect of SiC addition in electrolyte on the microstructure and tribological properties of micro-arc oxidation coatings on Al−Mg−Sc alloy [J]. Surface Topography: Metrology and Properties, 2021, 9: 035043.

[15] NARAYANAN SANKARA T S N S, LEE M H. Characteristics of microarc oxidation coatings deposited on magnesium using alkaline and acidic electrolytes in a single stage as well as using dual electrolytes in two stages [J]. Journal of Alloys and Compounds, 2016, 687: 720−732.

[16] TANG Ming-qi, FENG Zai-qiang, WU Xiang-yang, WANG Wen, LI Gang, YAN Zhen-wei, ZHANG Rui-zhu. Microarc oxidation coatings containing TiC and NbC on magnesium alloy [J]. Surface Engineering, 2020, 36: 1171−1179.

[17] XU Lu-yao, LIU Nai-yu, CAO Lei, WAN Yong. Influences of electrolytes on tribocorrosion performance of MAO coating on AZ31B magnesium alloy in simulated body fluid [J]. International Journal of Applied Ceramic Technology, 2021, 18: 1657−1669.

[18] WANG Zhi-hu, ZHANG Ju-mei, LI Yan, BAI Li-jing, ZHANG Guo-jun. Enhanced corrosion resistance of micro-arc oxidation coated magnesium alloy by superhydrophobic Mg−Al layered double hydroxide coating [J]. Transactions of Nonferrous Metals Society of China, 2019, 29: 2066−2077.

[19] YANG Hui-min, LIU Xian, SONG Xiu-li, YANG Tai-lai, LIANG Zhen-hai, FAN Cai-mei. In situ electrochemical synthesis of MOF-5 and its application in improving photocatalytic activity of BiOBr [J]. Transactions of Nonferrous Metals Society of China, 2015, 25: 3987−3994.

[20] JIANG Li, DONG Yan-mao, YUAN Yan, ZHOU Xing, LIU Ying-rui, MENG Xiang-kang. Recent advances of metal-organic frameworks in corrosion protection: From synthesis to applications [J]. Chemical Engineering Journal, 2022, 430: 132823.

[21] LI Bing-han, WANG S L, PAL S, SO P B, CHEN Guan-ying, HUANG Wei-jie, HSU Y L, KUO S Y, YEH Jui-Ming, LIN Chia-her. Versatile reactions on hydrophobic functionalization of metal-organic frameworks and anticorrosion application [J]. Microporous and Mesoporous Materials, 2021, 325: 111319.

[22] ZAKERNEZHAD M J, SEIDI S, MANOUCHEHRI M. Efficient ion separation from environmental and biological samples using a novel sorbent based on Ni-substituted ZIF-67: Optimization, equilibrium, kinetic, and thermodynamic study [J]. Industrial & Engineering Chemistry Research, 2022, 61: 1830−1840.

[23] RAMEZANZADEH M, RAMEZANZADEH B, MAHDAVIAN M, BAHLAKEH G. Development of metal-organic framework (MOF) decorated graphene oxide nanoplatforms for anti-corrosion epoxy coatings [J]. Carbon, 2020, 161: 231−251.

[24] ZHAO Yue, JIANG Fan, CHEN Yi-qing, HU Ji-ming. Coatings embedded with GO/MOFs nanocontainers having both active and passive protecting properties [J]. Corrosion Science, 2020, 168: 108563.

[25] GOTHANDAPANI K, GRACE A N, VENUGOPAL V. Mesoporous carbon-supported CO_3O_4 derived from Zif-67 metal organic framework (MOF) for hydrogen evolution reaction in acidic and alkaline medium [J]. International Journal of Energy Research, 2022, 46: 3384−3395.

[26] YU Guang-li, SUN Jian, MUHAMMAD F, WANG Peng-yuan, ZHU Guang-shan. Cobalt-based metal organic framework as precursor to achieve superior catalytic activity for aerobic epoxidation of styrene [J]. RSC Advances, 2014, 4: 38804−38811.

[27] SONG Guang-ling, ATRENS A, STJOHN D. Essential readings in magnesium technology [M]. Amsterdam: Springer, 2016: 565−572.

[28] SHI Xiao-ting, WANG Yu, LI Hong-yu, ZHANG Shu-fang, ZHAO Rong-fang, LI Guo-qiang, ZHANG Rong-fa, SHENG Yang, CAO Si-yue, ZHAO You-jun, XU Lin-na, ZHAO Ying. Corrosion resistance and biocompatibility of calcium-containing coatings developed in near-neutral solutions containing phytic acid and phosphoric acid on AZ31B alloy [J]. Journal of Alloys and Compounds, 2020, 823: 153721.

[29] LI Jian-peng, BIAN Yi-min, TU Xiao-hui, LI Wei, SONG Dong-dong. Influence of surface roughness of substrate on corrosion behavior of MAO coated ZM5 Mg alloy [J]. Journal of Electroanalytical Chemistry, 2022, 910: 116206.

[30] SAVAEDI Z, MIRZADEH H, AGHDAM R M, MAHMUDI R. Effect of grain size on the mechanical properties and bio-corrosion resistance of pure magnesium [J]. Journal of Materials Research and Technology, 2022, 19: 3100−3109.

[31] YE Jian-hui, BAI Shi-jie, HE Xin-ke, CHEN Jian-bin, XIE Chao. Effects of orientations, roughnesses, and cavities on stress-corrosion coupled damage in magnesium [J]. Crystals, 2022, 12: 635.

[32] WANG Nan-yi, LIU Yi, QIAO Zhi-wei, DIESTEL L, ZHOU Jian, HUANG Ai-sheng, CARO J. Polydopamine-based synthesis of a zeolite imidazolate framework ZIF-100 membrane with high H_2/CO_2 selectivity [J]. Journal of

Materials Chemistry A, 2015, 3: 4722−4728.

[33] BIEN C E, CHEN K K, CHIEN S C, REINER B R, LIN Li-chiang, WADE C R, WINSTON HO W S. Bioinspired metal–organic framework for trace CO_2 capture [J]. Journal of the American Chemical Society, 2018, 140: 12662−12666.

[34] WANG Hai-bo, WANG Yan-ling, REN Bao-yi, ZHANG Xue-jun. Study on corrosion resistance of Zn−Al alloy coated with zeolitic imidazolate framework-67 film in 3.5 wt.% NaCl solution [J]. Journal of Materials Engineering and Performance, 2020, 29: 1043−1050.

[35] GUO Xiu-ling, KONG Ling-jun, RUAN Y, DIAO Zeng-hui, SHIH K M, SU M H, CHEN Di-yun. Green and facile synthesis of cobalt-based metal–organic frameworks for the efficient removal of Congo red from aqueous solution [J]. Journal of Colloid and Interface Science, 2020, 578: 500−509.

[36] LIN K Y A, CHANG H A. Ultra-high adsorption capacity of zeolitic imidazole framework-67 (ZIF-67) for removal of malachite green from water [J]. Chemosphere, 2015, 139: 624−631.

[37] YAN Xue-cheng, JIA Yi, CHEN Jie, ZHU Zhong-hua, YAO Xiang-dong. Defective-activated-carbon-supported Mn−Co nanoparticles as a highly efficient electrocatalyst for oxygen reduction [J]. Advanced Materials, 2016, 28: 8771−8778.

[38] ADSUL S H, BAGALE U D, SONAWANE S H, SUBASRI R. Release rate kinetics of corrosion inhibitor loaded halloysite nanotube-based anticorrosion coatings on magnesium alloy AZ91D [J]. Journal of Magnesium and Alloys, 2021, 9: 202−215.

[39] CUI Lan-yue, GAO Ling, ZHANG Jing-chao, TANG Zhe, FAN Xiao-li, LIU Jia-cheng, CHEN Dong-chu, ZENG Rong-chang, LI Shuo-qi, ZHI Ke-qian. In vitro corrosion resistance, antibacterial activity and cytocompatibility of a layer-by-layer assembled DNA coating on magnesium alloy [J]. Journal of Magnesium and Alloys, 2021, 9: 266−280.

[40] WU Jia-hao, WU Hai-sheng, WU Liang, YAO Wen-hui, CHEN Yan-ning, SUN Li-dong, MA Yan-long, JIANG Bin, WANG Jing-feng, ATRENS A, PAN Fu-sheng. Preparation technology and properties of a thin anodic oxide composite film on the surface of an aluminum alloy foil [J]. Surface and Coatings Technology, 2022, 447: 128825.

[41] CHEN Yan-ning, WU Liang, YAO Wen-hui, ZHONG Zhi-yong, CHEN Yong-hua, WU Jia-hao, PAN Fu-sheng. One-step in situ synthesis of graphene oxide/MgAl-layered double hydroxide coating on a micro-arc oxidation coating for enhanced corrosion protection of magnesium alloys [J]. Surface and Coatings Technology, 2021, 413: 127083.

[42] AWAD K, YOUNG S, ASWATH P, VARANASI V. Interfacial adhesion and surface bioactivity of anodized titanium modified with SiON and SiONP surface coatings [J]. Surfaces and Interfaces, 2022, 28: 101645.

[43] ZHANG Xue-jun, ZHANG Yang, WANG Yan-ling, GAO Di, ZHAO Huan-xin. Preparation and corrosion resistance of hydrophobic zeolitic imidazolate framework (ZIF-90) film @Zn−Al alloy in NaCl solution [J]. Progress in Organic Coatings, 2018, 115: 94−99.

[44] WANG Li-da, ZONG Qiu-feng, SUN Wen, YANG Zheng-qing, LIU Gui-chang. Chemical modification of hydrotalcite coating for enhanced corrosion resistance [J]. Corrosion Science, 2015, 93: 256−266.

[45] SONG Yu-lai, WANG Hai-yang, LIU Qing, LI Gao-jie, WANG Sheng-wei, ZHU Xian-yong. Sodium dodecyl sulfate (SDS) intercalated MgAl layered double hydroxides film to enhance the corrosion resistance of AZ31 magnesium alloy [J]. Surface and Coatings Technology, 2021, 422: 127524.

[46] ZHANG Fen, LIU Zhen-guo, ZENG Rong-chang, LI Shuo-qi, CUI Hong-zhi, SONG Liang, HAN En-hou. Corrosion resistance of Mg−Al-LDH coating on magnesium alloy AZ31 [J]. Surface and Coatings Technology, 2014, 258: 1152−1158.

ZIF-67 膜在 AZ31 镁合金微弧氧化防腐涂层上的合成

陈勇花 [1,2]，吴 量 [1,2]，姚文辉 [1,2]，陈燕宁 [1,2]，
吴嘉豪 [1,2]，袁 媛 [1,2]，蒋 斌 [1,2]，Andrej ATRENS [3]，潘复生 [1,2]

1. 重庆大学 材料科学与工程学院 镁合金国家工程研究中心，重庆 400044；
2. 重庆大学 机械传动国家重点实验室，重庆 400044；
3. School of Mechanical and Mining Engineering, The University of Queensland, Brisbane Qld 4072, Australia

摘 要：为了提高 AZ31 镁合金的耐蚀性和金属有机骨架 MOFs 涂层的结合力，通过在 AZ31 镁合金微弧氧化(MAO)涂层上原位生长，制备 MAO/ZIF-67(微弧氧化/钴基金属有机骨架)复合涂层。结果表明，具有菱形十二面体的 ZIF-67 在 MAO 涂层表面均匀生长，与基体具有良好的附着力，这使得 MAO/ZIF-67 复合涂层具有良好的耐蚀性。实验证明，ZIF-67 能有效封闭 MAO 涂层的孔隙，增加腐蚀介质侵入路径的曲折度，显著提高镁合金的耐蚀性。此外，MAO 预处理使涂层具有强的附着力，这更有利于 ZIF-67 密封微孔。本研究对于降低 MOF 涂层在所有金属基底上的应用限制具有重要意义。

关键词：金属有机框架；ZIF-67；微弧氧化；防腐；涂层；Mg−Al−Zn 合金

(Edited by Wei-ping CHEN)